Article

A Comparative Study on the Choice of the Support in the Elaboration of Photocatalysts for the Photooxidation of Benzyl Alcohol under Mild Conditions

Lénaïck Hervé [ID], Svetlana Heyte [ID], Maya Marinova, Sébastien Paul [ID], Robert Wojcieszak [ID] and Joëlle Thuriot-Roukos *[ID]

Université de Lille, CNRS, Centrale Lille, Université d'Artois, UMR 8181-UCCS-Unité de Catalyse et Chimie du Solide, 59000 Lille, France; lenaick.herve@ircelyon.univ-lyon1.fr (L.H.); svetlana.heyte@univ-lille.fr (S.H.); maya.marinova@univ-lille.fr (M.M.); sebastien.paul@centralelille.fr (S.P.); robert.wojcieszak@univ-lille.fr (R.W.)
* Correspondence: joelle.thuriot@univ-lille.fr

Abstract: In the quest to combat global warming, traditional thermal chemistry processes are giving way to selective photocatalysis, an eco-friendly approach that operates under milder conditions, using benign solvents like water. Benzaldehyde, a versatile compound with applications spanning agroindustry, pharmaceuticals, and cosmetics, serves as a fundamental building block for various fine chemicals. This study aims at enhancing benzaldehyde production sustainability by utilizing photooxidation of benzyl alcohol. Gold nanoparticle-based catalysts are renowned for their exceptional efficiency in oxidizing bio-based molecules. In this research, Au nanoparticles were anchored onto three distinct supports: TiO_2, ZrO_2, and graphitic carbon nitride (g-C_3N_4). The objective was to investigate the influence of the support material on the selective photocatalysis of benzyl alcohol. In the preparation of g-C_3N_4, three different precursors—melamine, urea, and a 50:50 mixture of both—were chosen to analyze their impact on catalyst performance. After 4 h of irradiation at 365 nm, operating under acidic conditions (pH = 2), the Au photocatalyst on graphitic carbon nitride support synthesized using urea precursor ($Au@g$-$C_3N_{4(urea)}$) displayed the optimal balance between conversion (75%) and selectivity (85%). This formulation outperformed the benchmark $Au@TiO_2$, which achieved a similar conversion rate (80%) but exhibited lower selectivity (55%).

Keywords: photooxydation; g-C_3N_4; benzyl alcohol; benzaldehyde; gold nanoparticles; water solvent

1. Introduction

As the world grapples with escalating energy needs driven by expanding human activities, the reliance on fossil fuels remains pervasive across many regions. Unfortunately, this reliance carries the heavy burden of greenhouse gas emissions, with carbon dioxide levels consistently surging. NASA data [1] illustrates this concerning trend, revealing that in May 2003, atmospheric CO_2 concentrations stood at approximately 375 ppm and that, fast-forward 20 years to May 2023, this figure has spiked to 421 ppm. This relentless increase necessitates a concerted effort to diminish humanity's dependency on fossil resources, propelling the quest for innovative solutions. Among these solutions, biomass valorization, which can effectively harness an otherwise wasted resource and reduce significant CO_2 emissions, holds significant promise. Biomass, the organic matter accumulating solar energy within the planet's vegetation, can be a valuable source of material and energy. This source encompasses lignocellulosic biomass derived from agricultural residues, agro-industrial waste, and materials from the paper and textile industries, among others. These materials yield valuable sugars like xylose and glucose, which, in turn, provide a foundation for novel molecules and low-carbon or low-greenhouse gas emission fuels [2,3]. Carbohydrates have already been found to be extensively used in non-food applications, serving as crucial components in adhesives, additives, and more.

However, significant economic and scientific challenges must be addressed to unleash the full industrial-scale potential of this resource. Various strategies have been explored, including esterification and halogenation, but one of the most vital approaches involves the oxidation of carbohydrates and furanic compounds to produce bio-based organic molecules or intermediates applicable across a range of sectors, including pharmaceuticals, processing, cosmetics, and energy [2,4]. One illustrious bio-based chemical born from these processes is benzaldehyde, known for its almond-like aroma and found in apricot, cherry, and peach seeds, among other sources. Within the aromatic aldehyde family, benzaldehyde plays a prominent role in the perfumery industry, has earned "safe" status for food use from the American Food and Drug Administration (FDA), and serves as a precursor for various other aldehydes like cinnamaldehyde and methylcinnamaldehyde [5,6]. While benzaldehyde can be derived from bio-based raw materials, the predominant industrial method involves toluene chlorination followed by oxidation, often conducted at elevated temperatures (65–100 °C) [6,7], sometimes necessitating the addition of oxidizing agents like H_2O_2 or fluorinated solvents [8,9]. These harsh conditions pose risks and contribute to increased waste production. Researchers have been looking for new ways to generate a sustainable, environmentally friendly reaction to produce benzaldehyde. Photocatalysis is one of the green approaches explored in this paper to form benzaldehyde.

Photocatalysis was born by mimicking nature, especially with photosynthesis. In fact, the common points are numerous: light conversion, photo-charge transfer and separation, diffusion, and adsorption of reagents [10]. Developed in the 1960s with a first publication on the water splitting into H_2 and O_2 from a TiO_2 electrode [11], presently this new approach offers a transformative alternative to traditional catalysts, unlocking new possibilities and enhancing safety across a wide spectrum of applications, from environmental solutions to pharmaceuticals, energy, and chemistry [12–14]. Nevertheless, there remain several challenges that limit its application on a larger scale [10]. The first one is the improvement of the light use. Indeed, the principle of photocatalysis is based on the conduction of the electrons from the valence band (VB) to the conduction band (CB), thanks to the absorption of an energy light emission. Some strategies are currently in full development, but it is possible to cite the improvement of the capture of sunlight through the use of photocatalysts whose structure is inspired by plants. For instance, the hollow-structure nanoparticles can improve the capture light efficiency owing to the multireflection inside the sphere [15]. The most common semiconductors have a band gap in the range of 3–6 eV. After conversion, this corresponds to a radiation source in the UV range. However, the proportion of UV light in sunlight emission is very low (only 4–5%) [16]. Thus, another strategy is to develop new semiconductors that are more sensitive to sunlight emission (especially in the visible range). The last strategy for the improvement of light use consists of the enhancement of the photoelectron-hole separation. Holes are formed when the electrons are conducted to the CB; however, this state is unstable, and the electrons recombine with the holes to recover the initial stability. It was constated that on the bands, some redox reactions occur during this period. Unfortunately, this recombination is too fast; thus, the photocatalytic efficiency is low [17]. Always inspired by photosynthesis, researchers try to improve the redox capacities by constructing photocatalysts with heterojunctions. A second challenge is to optimize the catalytic reaction process by improving the mass transfer mechanism between the substrate molecules and the active sites. Mesoporous materials (i.e., TiO_2 [15]) possess ordered and tunable pores along with a high specific surface area. This ensures good accessibility and rapid mass transfer to active centers [18]. Moreover, it is necessary to ensure the durability of the photocatalysts, which is a key issue that limits their applications. In fact, after several long-term irradiation, the photocatalyst is poisoned due to the adsorption on the surface of products or by-products. As a result of this clogging, the photocatalyst loses its activity, either the inhibition of the photon absorption and/or the inability of the substrate molecules to diffuse to the active sites [19]. Finally, the last challenge consists of the enhancement of the photocatalyst activity. For this purpose, two strategies are mainly explored: the preparation of materials with a single-crystal facet

and the integration of a supported co-catalyst. Crystal facets exhibit high surface energy as a consequence of high photocatalytic activity because of good separation of the charge carriers and abundant active surface sites [10]. This strategy enables the enhancement of the photocatalytic activity at the atomic scale by preparing material with a single and specific facet, such as TiO_2 demonstrated the best photocatalytic activity with the (001) facet than the others [20]. The second strategy involves combining a semiconductor with a co-catalyst, which adapts the band structure, improves the interfacial charge transfer, and provides more active centers. This alternative approach allows the enhancement of the photocatalytic properties of semiconductor materials [10]. Frequently, noble metals are used as co-catalyst [21], permitting the facilitation of the interfacial migration of charge thanks to the formation of a Schottky barrier at the interface between the semiconductor and the co-catalyst [22]. However, this strategy will be developed and provided through this study.

Titanium dioxide (TiO_2) and its variants stand out, cherished for their stability, cost-effectiveness, and minimal environmental and human health risks [23,24]. TiO_2 has already achieved widespread use, particularly in photovoltaic power generation [25]. Since the 1950s, carbon-based materials, including fibers, nanotubes, graphene, and mesoporous structures, have revolutionized numerous fields. These materials form robust covalent bonds, enhancing properties such as strength, density, hardness, and electronic conduction capabilities. Among carbon-based semiconductor materials, carbon nitride graphite (g-C_3N_4) emerges as a promising contender [26]. Discovered in the 1830s [27], g-C_3N_4 is comprised primarily of carbon, nitrogen, and traces of hydrogen and is a polymeric material characterized by the heptazine motif. This structural feature confers upon carbon nitride graphite excellent electron conduction properties, thanks to its conjugated π-bonds and nitrogen's non-bonding doublet [28]. As a result, g-C_3N_4 emerges as an exceptional photocatalyst with high photoelectric properties and an appropriate band gap for visible light (450 nm) [29], distinguishing it from TiO_2, which predominantly absorbs near-UV light (380 nm) [30]. Moreover, this carbon-based polymer can be produced from bio-sourced precursors rich in nitrogen and carbon, like melamine and urea, using a cost-effective and solvent-free process [31]. Already, g-C_3N_4 has found utility in numerous applications, from hydrogen production [32–34], to water treatment through the photodegradation of pollutants [35–37] and nitrogen oxide (NO) removal [38,39].

In the context of photooxidation, various studies have delved into the photocatalytic transformation of benzyl alcohol into benzaldehyde, employing a range of organic solvents such as DMSO, benzotrifluoride, and acetonitrile [40–42]. While water has also been employed as a solvent by different researchers, it is important to note that these endeavors have often resulted in limited conversion of benzyl alcohol or modest yields of benzaldehyde [43,44]. Furthermore, some photocatalytic systems have raised concerns about potential hazards. For instance, a study involving a CdS/TiO_2 photocatalyst demonstrated promising results with an approximate conversion rate of 60%. Unfortunately, the degradation of this catalyst can result in the release of highly toxic Cd^{2+} ions into the solvent, posing a significant environmental risk [45,46]. On the other hand, g-C_3N_4 has gained recognition for its safer profile and has been the subject of numerous investigations. It has been reported that while g-C_3N_4 exhibits low conversion rates of benzyl alcohol, it excels as a highly selective photocatalyst for benzaldehyde [47,48]. This work focuses on the development of a promising, efficient, and selective photooxidation method for converting benzyl alcohol into benzaldehyde. This transformation is achieved using an aqueous substrate solution under mild temperature and pressure conditions, with the added advantage of employing energy-efficient LED technology as the light source.

Furthermore, this study places special emphasis on the deposition of gold nanoparticles (NPs) onto g-C_3N_4, a critical aspect that has been thoroughly investigated. Additionally, different precursors have been employed in the preparation of g-C_3N_4, and meticulous attention has been paid to discerning potential distinctions among these various precursors.

The outcomes of these investigations are thoughtfully compared with the performance of TiO_2 and ZrO_2, providing valuable insights into the photocatalytic process.

2. Materials and Methods

2.1. Chemicals

The following chemical compounds were used in the different next sections: ZrO_2 (99%), TiO_2 ($\geq$98%), $HAuCl_{4(sol.)}$ (30 wt.%, 99.99%), PVA (MW: 9000–10,000), sodium boron-hydride ($NaBH_4$, $\geq$96%), urea (99–100.5%), melamine (99%), benzyl alcohol (99.8%, anhydrous), benzaldehyde (99.5%), formic acid ($\geq$95%) were all provided from Sigma-Aldrich (Saint-Louis, MO, USA); nitric acid (HNO_3, 67–69%), sulfuric acid (H_2SO_4, 93–98%) and hydrochloric acid (HCl, 35–37%) were provided from SCP Science (Baie d'Urfé, QC, Canada).

2.2. Preparation of Gold NPs on $M_{(M=Zr,Ti)}O_2$

The catalysts containing 2 wt.% gold were prepared by the sol immobilization method of gold nanoparticles on TiO_2 and ZrO_2, following a method reported in our previous works [49]. The metal loading of 2 wt. % permits good dispersion of metallic nanoparticles and guarantees the optimal charge separation [49,50]. In brief, in 200 mL of distilled water, 115 mg of $HAuCl_4$ solution were added, followed by the addition of a 1.2 mL of 2 wt.% PVA solution. After agitation for 2–3 min, a 5 mL of 0.1 M sodium boronhydride solution was added to reduce gold ions. For efficient reduction of gold ions and immobilization of gold nanoparticles on support, the molar ratio of Au:$NaBH_4$ was 1:5. The solution was agitated for 30 min, then 1 g of titanium oxide was introduced. The suspension was agitated for 2 h and finally filtrated on Büchner, washed with hot distilled water (60 °C) (3 × 200 mL) and ethanol (1 × 200 mL) and dried in an oven overnight at 60 °C.

In the case of zirconium oxide, the same procedure was applied as for TiO_2; however, after adding the support, the pH of the suspension was adjusted at a pH around 3, from an acid solution stock (HNO_3, 1 M). All the routes were repeated three times to guarantee the accuracy of the method.

2.3. Preparation of the Carbon Nitride Graphite Carrier (g-C_3N_4)

A previous method reported in [51] was used to prepare the supports. Moreover, three carbon-based carriers were prepared with different carbon/nitrogen precursors: urea, melamine, and a mix of both (50:50, wt:wt). Then, they were crushed in an agate mortar. For each precursor, 10 g were placed in a porcelain crucible and put in a calcination oven. The powders were correctly closed with another porcelain crucible and heated at 550 °C (10 °C/min) for 3 h, under static air. Each of the supports was prepared in triplicate.

2.4. Preparation of the Gold NPs supported on Carbon Nitride Graphite

The prepared supports were loaded with 2 wt.% gold NPs by a simple and modified method previously reported in [52,53]. From the carbon nitride support, 500 mg were dispersed homogeneously in 50 mL of distilled water by an ultrasonic bath for 1 h. Then, a $HAuCl_4$ solution was added (57.5 mg), followed by the reduction step with a $NaBH_4$ solution in the same proportion as described in Section 2.2. Afterward, the pH solution was adjusted to 2 by adding a nitric acid solution at 1 M, and the suspension was mixed for 2 h. After 2 h, the solution was filtrated on a Büchner. The catalyst was washed with distilled water until the pH increased at 7 and ethanol (1 × 200 mL), and finally dried overnight in an oven at 60 °C. The synthesis was repeated three times.

2.5. RAMAN Spectroscopy

The Raman spectra were recorded on Xplora^{TM} Raman confocal Microscope (HORIBA Jobin Yvon, Kyoto, Japan) equipped with a multiple-wavelength laser. The excitation wavelength used in this study was 785 nm sourced by diode laser with a laser power of 90 mW. A 50× (LWD: long working distance; NA: 0.50) objective was used to focus the laser beam down to a 1.9 μm-diameter spot on the sample. The scattered light was collected

by the same objective and passed through a notch filter to minimize Raleigh's scattered components before detection. The Raman is equipped with a CDD detector cooled with a Peltier cooling (213 K). The Raman scattered light was collected in the spectral range 100–1200 cm^{-1}. To improve the spectra resolution, a 600 gr/mm grating was used and acquired one time for 120 s.

2.6. X-ray Diffraction (XRD)

Powder X-ray diffraction patterns were obtained using a D8 Advance X-ray powder diffractometer (Bruker, Karlsruhe, Germany) equipped with a Cu Kα_1 radiation source (λ = 1.5406 Å) operating at 40 kV and 40 mV and a detector 1D Lynx eyes detector. The intensity data were collected over a 2θ range of 10–70° with a step size of 0.014° using a counting time of 0.1 s per point. Crystalline phases were identified by comparison with the reference data from ICDD files. Finally, the crystallite size was evaluated using the Scherrer equation:

$$\tau = \frac{K\lambda}{\beta \cos(\theta)} \tag{1}$$

where: τ, crystallite size (Å); K, shape factor (no dimension); λ, the X-ray wavelength (1.5406 Å); β, the line broadening at half of the maximum intensity (FWHM) (rad); θ, Bragg angle (°).

2.7. Organic Analyzer: CHNS

To determine the organic elements, the Flash Smart analyzer (Thermo Scientific, Waltham, MA, USA) was used. For CHNS determination, the samples were weighted in tin containers and introduced into the combustion reactor. The reactor is filled with copper oxide followed by wire-reduced nickel and maintained at 950 °C. It operates with dynamic flash combustion of the sample. The N, C, H, and S were detected as N_2, CO_2, H_2O, and SO_2, respectively. The resulted gases were separated on a packed column (Hayesep 2 m $\times$ 6 mm) heated at 60 °C in an oven and detected by a TCD (thermal conductivity detector). Each sample was analyzed three times to obtain reliable results.

2.8. X-ray Fluorescence

The relative contents of titanium, zirconium, and gold were determined with the use of an energy dispersive micro-X-Ray Fluorescence spectrometer M4 TORNADO (Bruker, Berlin, Germany). For sample characterization, the X-rays Rhodium equipped with a polycapillary lens was used. The detector used was a Silicon-Drift-Detector Si(Li) with <145 eV resolution at 100,000 cps (Mn Kα) and cooled with a Peltier cooling (253 K). The elements that can be measured by this instrument unit range from sodium (Na) to uranium (U). Quantitative analysis was conducted using fundamental parameters (FP) (standard less). The measurement was made under a vacuum (20 mbar). As elements are present in stoichiometric compounds formula TiO_2 and ZrO_2 for Titanium and Zirconium Oxide, respectively, this knowledge was used for quantification of the weight percent of each element. For analysis, a few milligrams of dried and ground samples were placed in a multi-well plate of thickness of 2 mm for each well. For each sample, 36 points were measured in order to cover the sample surface with a spot size of 200 μm for each point.

2.9. ICP-OES

The elemental analysis was performed by inductively coupled plasma-optic emission spectroscopy 720-ES ICP-OES (Agilent, Santa Clara, CA, USA) with axially viewing and simultaneous CCD detection. The quantitative determination of metal content in the catalysts was made based on the analysis of certificated standard solutions. The ICP Expert™ software (version 2.0.4) provides the concentration of metal in the sample, allowing estimating the weight percentage of gold (Au). All the analyses were performed 40 min after the spectrometer was turned on to achieve a stable plasma as well as a constant and reproducible sample introduction.

The sample preparation was made by dissolving 10 mg of dried and ground samples catalyst in concentrated aqua regia solution (HNO$_3$:HCl) (1:3, *v:v*). All the sample solutions were stirred overnight in an ultrasonic cleaner heated up to 80 °C and diluted in 20 mL of ultrapure water before being analyzed by ICP-OES.

2.10. UV-Visible Spectroscopy Analyses

The analyses realized on UV-Vis were conducted on a Lambda 650 apparatus of Perkin–Elmer (Shelton, CT, USA), on a wavelength scale between 220 and 870 nm. For the analysis needs, the samples were crushed and conditioned in a quartz cuvette of 1 mm path length before being carried in the apparatus sample holder. The energies corresponding to the wavelengths were calculated from the Plank-Einstein relation, such as:

$$\mathbb{E} = h \times \nu = h \times \frac{c}{\lambda} \tag{2}$$

where: $\mathbb{E}$, Energy of the incident emission (converted in eV from the elementary charge: $\approx 1.60 \cdot 10^{-19}$ J = 1 eV); h, Plank constant ($\approx 6.63 \cdot 10^{-34}$ J s) ; c, celerity of light ($\approx 3 \times 10^8$ m s^{-1}); λ, wavelength of the incident light (nm).

2.11. Transmission Electronic Microscopy (TEM)

The TEM has been performed on a Thermo Fisher Scientific (Waltham, MA, USA) G2-20 twin TEM with LaB$_6$ filament operating at 200 kV. The bright field images have been acquired in parallel electron beam with a 20 μm diffraction aperture and using a Gatan CCD camera.

2.12. Photocatalytic Reactions

The screening of the catalysts was realized for the photooxidation of benzyl alcohol to benzaldehyde as the main product. The reactions were performed using a LightSyn Illumin8 (ASYNT, Cambridgeshire, UK) photoreactor, which was dedicated to studying up to eight reactions per batch. Each quartz tube (8 mL) is equipped with its own LED illumination (10 W) at 365 nm. Borosilicate glass tubes used for the photocatalytic tests are highly transparent to UV radiation; however, a slight attenuation effect can affect the intensity of the light passing through it. Moreover, due to the specificity of the equipment, it was impossible to conduct specific measurements of this attenuation. Thus, the actual power reaching the reaction mixture was likely to be slightly lower than the rated power of the LEDs ($\leq$10 W).

The tubes were loaded with 25 mg of catalysts or supports, then filled with an aqueous solution of benzyl alcohol (5 mL, 24.7 mmol/L). Based on the results of the work on the benzyl alcohol photooxidation [54], the media were first acidified to pH 2 by adding sulfuric acid. Finally, the reactions were conducted for 4 h, with stirring at 600 rpm, under atmospheric pressure, and without temperature control (increased to 40 °C). After the reaction, the samples were filtrated on nylon filters (0.2 μm) and analyzed on a UHPLC chromatograph (Shimadzu, Kyoto, Japan) described below.

Moreover, conversion (C), selectivity (S), and yield (Y) were calculated from the following equations, with BA representing benzyl alcohol and BAL benzaldehyde:

$$C(\%) = [(n_{\text{BA}_0} - n_{\text{BA}})/n_{\text{BA}_0}] \times 100; \tag{3}$$

$$S(\%) = [n_{\text{BAL}}/(n_{\text{BA}_0} - n_{\text{BA}})] \times 100; \tag{4}$$

$$Y(\%) = [n_{\text{BAL}}/n_{\text{BA}_0}] \times 100 \tag{5}$$

where n_{BA_0} represents the initial quantity of BA (mmol), n_{BA} and n_{BAL} the quantities determined of BA and BAL, respectively, (mmol) after the reaction.

2.13. HPLC Analysis

HPLC-DAD liquid chromatograph from Shimadzu equipped with diode array detector (DAD) SPD-M20A (λ = 190–800 nm) and binary pumps LC-30AD were used for the quantitative determination of the products. HPLC analysis is carried out using an LC column polar column (C18) Kinetex$^©$, 100 Å, 2.6 μm, 100 × 2.1 mm, operated at 22 °C. Analysis is carried out at 197 and 243 nm, detectors cell temperature 22 °C. A gradient elution was used between water with 0.1% formic acid (A) and acetonitrile with 0.1% formic acid (B), with a total flow at 0.6 mL/min.

3. Results and Discussion

3.1. Gold NPs on Titanium and Zirconium Oxide

Figure 1 displays the Au@TiO$_2$ and Au@ZrO$_2$ X-ray diffraction patterns. For TiO$_2$, the XRD pattern shows the presence of anatase and rutile phases. Gold NPs were not observed on TiO$_2$ and ZrO$_2$ catalyst patterns due to their high dispersion and small particle size [50]. The symbols A and R indicate anatase and rutile phases of TiO$_2$, respectively. The anatase phase shows 3 major peaks at 2θ: A 25° (101), A 37.6° (004) and A 47.9° (200). Minor peaks can be also observed for anatase and rutile as follows: R 27.4° (110), R 36° (101), A 36.9° (103), A 38.48° (112), R 39.2° (200), R 41.1° (111), A 53.8° (105), A 54.2° (211), A 55° (211), R 56.57° (220), A 62° (213), A 62.6° (204) and R 69° (301). The Miller Indices were assigned according to the PDF Card: 00-021-1272 for Anatase and PDF Card: 00-021-1276 for Rutile. The ZrO$_2$ pattern reveals only the Baddeleyite phase when comparing the main diffraction peaks and hkl at 28° (−111), 31.4° (111) and 50.1° (022) with those of the PDF Card: 00-037-1484) from ICDD. These peaks correspond to the monoclinic P2$_1$/c crystal system as reported by [55].

(**a**)
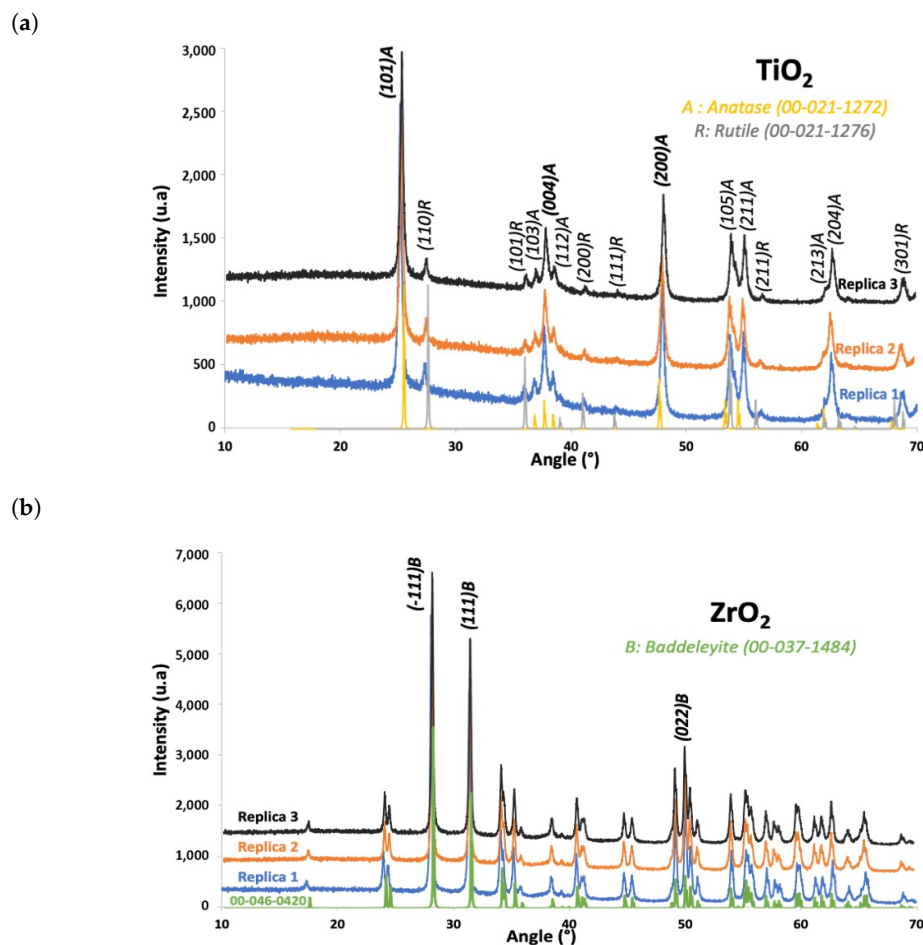

(**b**)

Figure 1. XRD patterns of the catalysts: (**a**) Au@TiO$_2$ replicas. (**b**) Au@ZrO$_2$ replicas.

The XRF results presented in Table 1 reveal the quantity of gold loaded onto each oxide support. While the expected gold content was 2 wt.%, an average of 2.27 wt.% of gold nanoparticles (NPs) was quantified on TiO_2. Conversely, only 1.89 wt.% of gold NPs was measured on ZrO_2. The deviation from the target gold could be attributed to the "matrix effect" of the metal oxide [56], where the support's quantity is either underestimated or overestimated, consequently affecting the gold measurement. In the case of TiO_2, it was likely underestimated, while for ZrO_2, the gold content might have been overestimated based on the results of [56], which could have resulted in a total percentage exceeding 100% or falling short.

Table 1. Gold content on Titanium and Zirconium Oxide from the XRF analyses.

| Replicas	Au Content on TiO_2 [wt.%]	Au Content on ZrO_2 [wt.%]
Replica 1	2.30	1.88
Replica 2	2.29	1.88
Replica 3	2.24	1.69
Average	2.27	1.89
Std. Dev.	0.02	0.09
Rel. Std. Dev. [%]	1.08	4.74

Notably, the comparison between replicates for both supports highlights that the relative standard deviation of gold content is low (1.08% on TiO_2 and 4.74% on ZrO_2), confirming the validity of the respective synthesis methods.

3.2. Carbon Nitride Graphite (g-C_3N_4) Support

Figure 2 represents the XRD patterns and Raman spectra of the supports obtained from the melamine, urea, and mixed precursors. XRD patterns (Figure 2a) obtained fit perfectly with the graphitic carbon nitride model (PDF-Card:00-066-0813). On the one hand, the patterns show an important peak at 27.4° (002), extremely characteristic of the stacking of the aromatic rings [56]. This is confirmed by the stacking distance estimates around 0.325 nm for the three g-C_3N_4 precursors. Thus, the results are close to the stacking distance value of graphitic materials (0.34 nm) [57]. Although the peak around 13° (100) is related to the repetition in the plan of the tri-s-triazine motif, the distance is evaluated to be 0.685 nm for all graphitic supports, which is consistent for this type of pattern [57,58].

On the other hand, the intensity of the main peak is not the same for all precursors. According to the Scherrer equation, the crystallite size was evaluated on the most intense peak (002) of the g-C_3N_4 phase: $\tau_{g-C_3N_4(melamine)} = 77.0$ Å, $\tau_{g-C_3N_4(mix)} = 55.1$ Å and $\tau_{g-C_3N_4(urea)} = 26.0$ Å. Consequently, the carrier acquired from melamine seems to be more graphitized than that obtained from the mixture of melamine and urea or even from urea alone. This implies that the more complex the precursor, the more accessible and faster it is to graphitize the carbon nitride. This phenomenon is due to the mechanism by which melamine is an intermediate in the urea calcination process [59].

Raman spectra in Figure 2b, provide the vibration of the graphitic carbon nitride. As shown on the spectra, several signals at low Raman shift (400–600 cm^{-1}) are assigned to the breathing mode of heptazine. Furthermore, the 4 main peaks at around 700–970 cm^{-1} (¤) correspond to the breathing mode of heptazine and the final peak, $\approx$1220 cm^{-1} ($\triangle$), is attributed to the stretching modes of C-N and C=N bonds within the heterocycle [60]. On the other hand, the organic elements analyses confirm that for the three carbon nitride supports, the same carbon:nitrogen (C:N) mass ratio ≈ 0.58 (Table 2); thus, the molar ratio is approximately 0.68. This ratio is lower than expected (0.75) due to the presence of hydrogen traces at the surface of the support. However, the most important loss is caused by the release of carbon gases during the process. These various results confirm the correct crystallinity and structure of all the carbon nitride supports prepared.

(**a**)

(**b**)
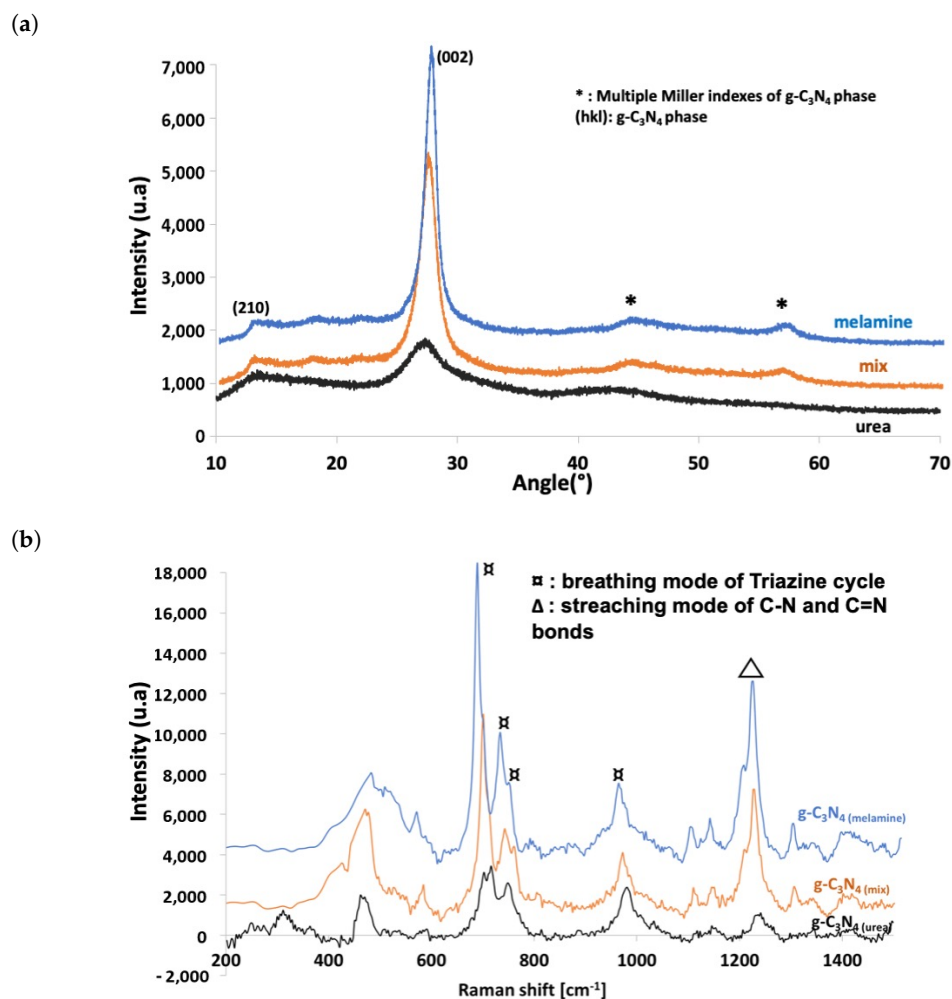
Figure 2. g-C_3N_4 supports characterization: (**a**) XRD patterns. (**b**) Raman spectra.

Table 2. Organic elements analyses of g-C_3N_4 supports prepared from different precursors.

Supports	C (wt.%)	N (wt.%)	H (wt.%)	C:N
g-$C_3N_{4(melamine)}$	35.15	60.62	1.72	0.5798
g-$C_3N_{4(mix)}$	34.89	60.19	1.68	0.5796
g-$C_3N_{4(urea)}$	33.08	56.84	1.77	0.5820

3.3. Gold NPs on Graphite Carbon Nitride Carrier

The XRD analyses have confirmed two critical aspects: the preservation of the crystalline structure within the graphitic support and the effective immobilization of the gold nanoparticles, as illustrated in Figure 3a. The XRD pattern can be accurately indexed to the main peak at approximately 38° (111), along with two additional peaks at approximately 44° (200) and approximately 65° (220). These reflections are indicative of a face-centered cubic (fcc) crystal structure consistent with the PDF Card reference: 00-066-0091. Notably, variations in the degree of graphitization stemming from the different precursors have discernible impacts on the crystallinity of the nanoparticles. Consequently, employing the Scherrer equation, the crystallite sizes were calculated based on the most intense peak (111) within the gold phase: $\tau_{Au@g-C_3N_4(melamine)}$ = 86 Å, $\tau_{Au@g-C_3N_4(mix)}$ = 70.6 Å and $\tau_{Au@g-C_3N_4(urea)}$ = 58.8 Å. Because of the previous results for the crystallite sizes of the supports, there is a correlation between the progress of the graphitization process and the emergence of crystallinity in the gold NPs. The observed results regarding the crys-

tallite sizes of the supports suggest a noteworthy correlation between the advancement of the graphitization process and the development of crystalline structures in the gold nanoparticles. In terms of the Raman spectroscopy findings, as depicted in Figure 3b, it is evident that the carbon support remains structurally intact, as indicated by the presence of characteristic peaks in the range of 700–970 and 1220 cm^{-1}. Moreover, a comparison of the Raman spectra both before (Figure 2b) and after the immobilization of the gold nanoparticles underscores the impact of the supported nanoparticles. Notably, the introduction of gold nanoparticles results in a reduction in the intensity of all spectral peaks, eventually leading to an almost indiscernible spectrum, exemplified by g-C$_3$N$_{4(urea)}$. The gold nanoparticles serve as a shielding agent, diminishing the propensity of the support bonds to vibrate. ICP analysis yielded a gold concentration of approximately 1.95 wt%. Furthermore, the synthesized catalysts underwent evaluation using an organic analyzer, which revealed a consistent C:N mass ratio of approximately 0.58 across all support types. This finding indicates the absence of any detectable loss of elements, affirming that the supports remained structurally sound during the immobilization of the nanoparticles. Taken together, the characterization results provide assurance that the gold nanoparticles supported on g-C$_3$N$_4$ are effectively immobilized, with the anticipated metal loading, all while maintaining the structural integrity of the support throughout the process.

(**a**)

(**b**)
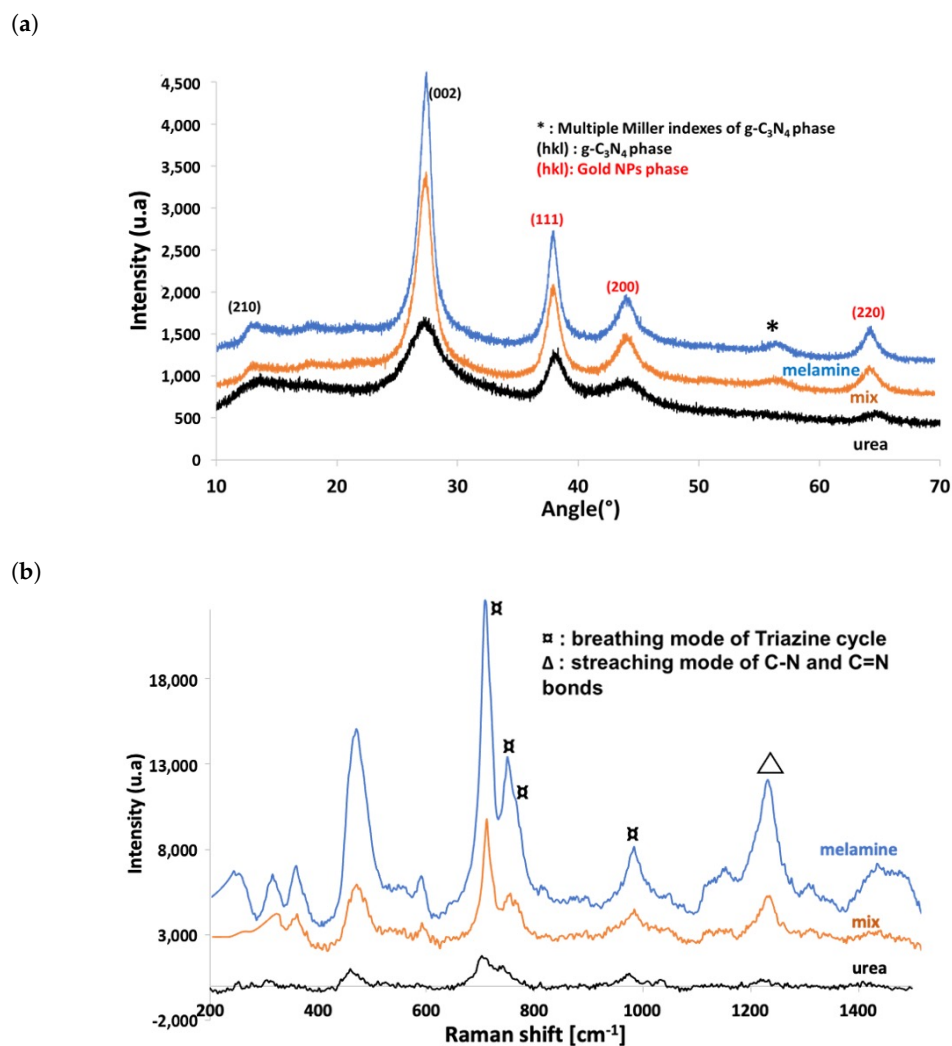
Figure 3. Au@g-C$_3$N$_4$ (**a**) XRD patterns with the g-C$_3$N$_4$ (black) and Gold NPs (red) phases. (**b**) Raman spectra.
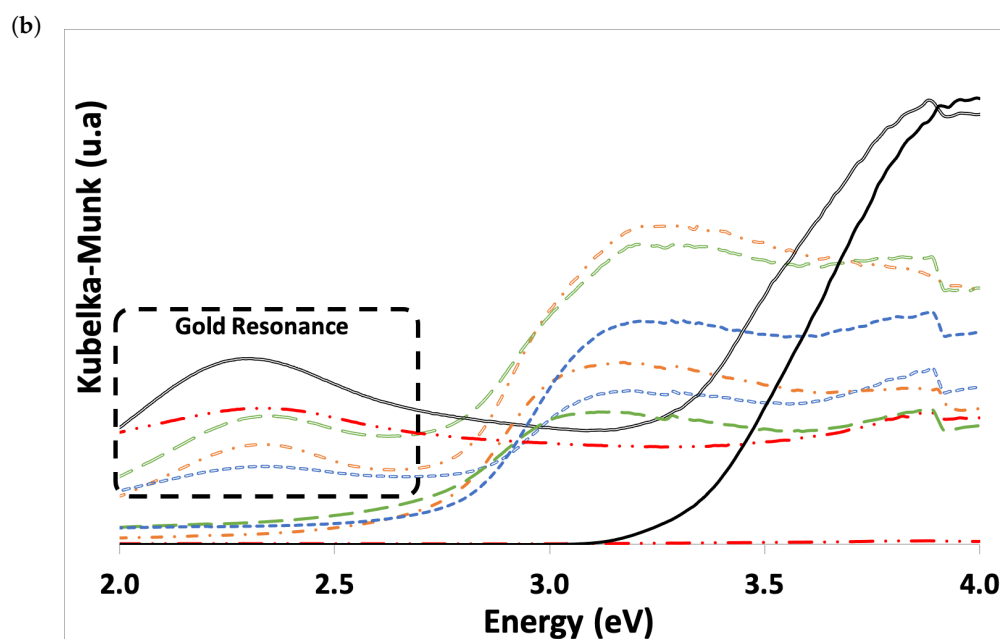
3.4. UV-Visible Spectroscopy Analyses

The Diffuse Reflectance UV-Visible (DR UV-Vis) spectra, depicted in Figure 4, reveal distinctive absorption patterns for the various supports and catalysts under examination. When considering the supports (Figure 4a), TiO$_2$ exhibits the classic near-UV absorption at around 390 nm. In contrast, the carbon nitride supports display a notable shift towards the blue region, with absorption occurring at approximately 450 nm. For zirconium oxide, the absorption is observed in the far UV range, at approximately 250 nm. Upon immobilization of the gold nanoparticles, all the catalysts exhibit a distinct peak at 530 nm, indicative of the characteristic surface plasmon resonance of gold [57,60]. Notably, the introduction of gold nanoparticles enhances the absorption capacity of the bare supports in the visible range. Furthermore, the energy gap of the samples was determined based on the Tauc plots (Figure 4b) and is summarized in Table 3. Across all the catalysts synthesized, the addition of gold nanoparticles results in a reduction of the bandgap energy when compared to the corresponding bare supports. As an example, for g-C$_3$N$_{4(urea)}$, the bandgap energy decreases from 2.78 eV before immobilization to 2.66 eV after synthesis, representing a reduction of 0.12 eV. Similar observations were made for the other carbon nitride supports, albeit with differing magnitudes (g-C$_3$N$_{4(melamine)}$: 2.73 to 2.69 eV and g-C$_3$N$_{4(mix)}$: 2.62 to 2.53 eV). In the case of TiO$_2$, the bandgap energy decreases from 3.34 eV to 3.15 eV. These findings pave the way for conducting photocatalytic tests, particularly under a near-UV light source.

Table 3. Energy gap of the supports and the catalysts.

Supports	Energy Gap (eV)	Catalysts	Energy Gap (eV)
TiO$_2$	3.34	Au@TiO$_2$	3.15
ZrO$_2$	5.10	Au@ZrO$_2$	4.94
g-C$_3$N$_{4(melamine)}$	2.73	Au@g-C$_3$N$_{4(melamine)}$	2.69
g-C$_3$N$_{4(mix)}$	2.62	Au@g-C$_3$N$_{4(mix)}$	2.56
g-C$_3$N$_{4(urea)}$	2.78	Au@g-C$_3$N$_{4(urea)}$	2.66

Figure 4. *Cont.*

(b)
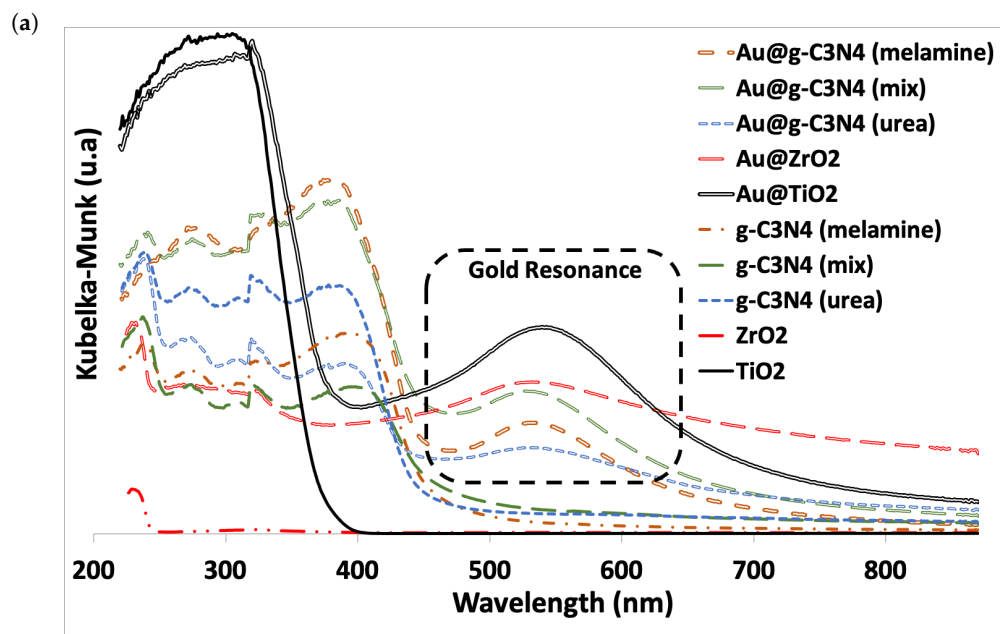
Figure 4. (**a**) DR UV-Vis spectra of the supports and the catalysts. (**b**) With the corresponding Tauc plots.

3.5. Microscopy Analyses of Gold NPs Supported on g-C$_3$N$_4$ (TEM)

Figure 5 depicts the Transmission Electronic Microscopy (TEM) images and the particle size distributions for Au NPs deposited on the different g-C$_3$N$_4$ nature. All the particles deposited on the different sources of g-C$_3$N$_4$ are characterized by a spherical shape, with particle size <10 nm. Nevertheless, the heterogeneity is not the same according to the source of the carbon nitride precursor. Indeed, the Au@g-C$_3$N$_{4(mix)}$ is the most heterogenous photocatalyst, with the presence of large aggregates (>25 nm), also, in average the particles size is superior (7.25 ± 1.74 nm) with an assessment of 250 particles. For Au@g-C$_3$N$_{4(melamine)}$ and Au@g-C$_3$N$_{4(urea)}$, the formation of some aggregates was reported too, even though they are smaller than those of Au@g-C$_3$N$_{4(mix)}$ (13.5 to 20 nm), otherwise the size of the Au particles is practically identical: 5.07 ± 1.39 nm and 5.24 ± 1.30 nm, respectively.

3.6. Photocatalytic Tests

In the realm of photocatalysis, the choice of the solvent plays a pivotal role in the selective oxidation of alcohols to their corresponding aldehydes. Several organic solvents have undergone thorough investigation in this regard, including acetonitrile, toluene, and deep eutectic solvents [61–63]. However, aligning with the principles of green chemistry, which advocate for the use of safer solvents [64], the most favorable option remains water. Consequently, the photocatalytic experiments were conducted in aqueous media. Nevertheless, when employing water as the solvent, it becomes essential to carefully control the pH to prevent overoxidation or substrate degradation. This is particularly critical in light of the potential hydroxyl radical attack resulting from the interaction between HO$^-$ and photogenerated holes [64]. The zero-point charge of the carbon nitride support has been documented in the literature as pH = 2.1 [65]. At lower pH levels, the abundance of H$^+$ ions in the solution leads to their adsorption on the catalyst's surface, competing with the substrate for active sites, mainly through interactions with nitrogen atoms. In contrast, at pH values exceeding the zero-point charge, the catalyst's surface becomes negatively charged, which, in turn, promotes interactions with the chemicals to be catalyzed. These interactions are facilitated through the formation of hydrogen bonds, such as O—H$\cdots$N or O—H$\cdots\pi$ bonds [65,66]. The work [54] conducted extensive investigations into various pH conditions (ranging from pH = 2, 3, to 5.6) during the photooxidation of benzyl alcohol

to benzaldehyde under an inert atmosphere, with irradiation at 390 nm. Thus, the pH was adjusted to 2 using H_2SO_4 to maintain the zero-point charge for g-C_3N_4.
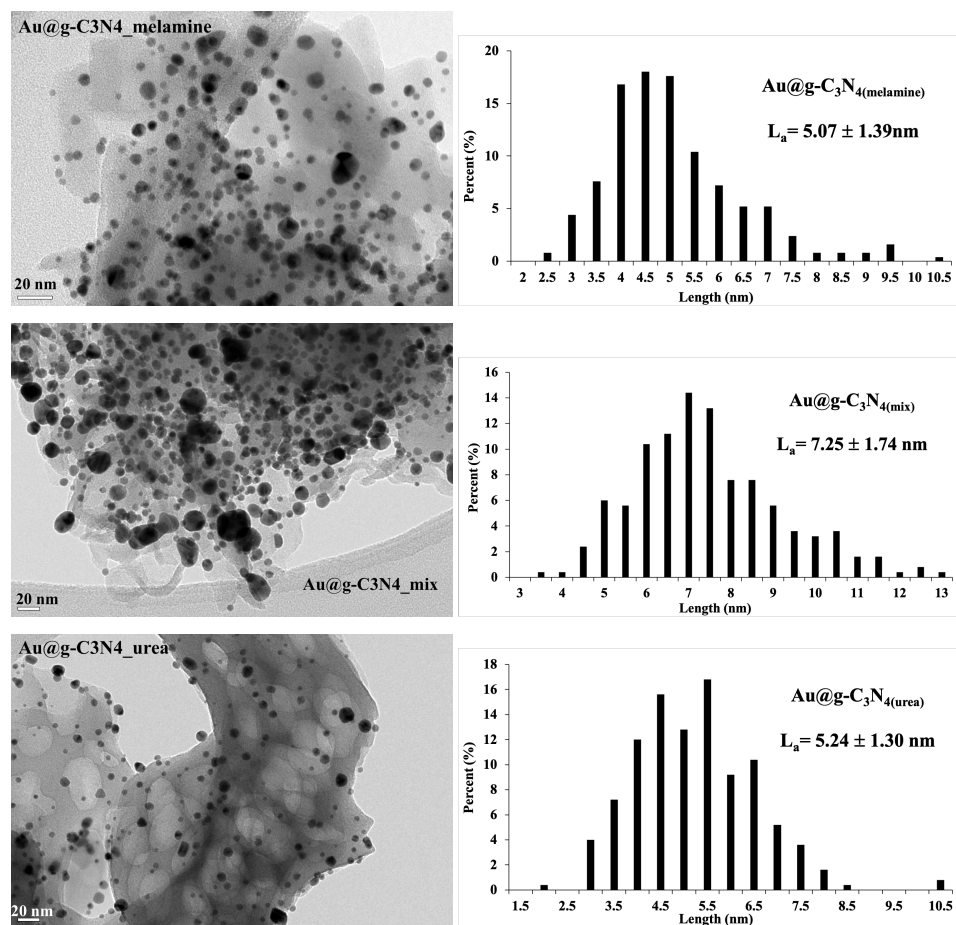
**Figure 5.** Typical TEM images and particle size distributions for Au NPs immobilized on the different precursors of g-C_3N_4.

To assess the pivotal role of the light source in photocatalytic activation, a control experiment without light illumination was conducted (Figure 6). Under identical conditions as previously detailed in Section 2 but in the absence of 365 nm irradiation, all the supports and catalysts exhibited markedly low activity. The maximum conversion of benzyl alcohol was around 12% for Au@TiO_2 and slightly exceeded 10% for the bare support. This indicates that, even in the absence of irradiation, both TiO_2 and Au@TiO_2 display minimal catalytic activity. In contrast, the carbon nitride supports and catalysts yielded conversions of less than 4%. Notably, all samples exhibited the formation of benzaldehyde on the chromatogram, although the quantities obtained fell below the quantification limit.

Following confirmation of the essential role of light in this reaction, photocatalysis tests were conducted, and the results are shown in Figure 7, which illustrates the outcomes following the triple testing of photocatalysts and bare supports. It is worth highlighting that, as per TEM analysis, C_3N_4-based catalysts exhibited no discernible difference in particle size, with a mean size of 5 nm and wide distribution ranging from 2 to 10 nm. This underscores the validity of comparing the activity of g-C_3N_4 catalyst, which is the central focus of this study. In our research, Au@TiO_2 and Au@ZrO_2 catalysts were exclusively selected as benchmark catalysts. TEM analysis revealed a mean particle size of 3 nm for both, with a distribution spanning from 1 to 5 nm [50]. Notably, all catalysts exhibited particle sizes below 10 nm when considering the distribution. Consequently, all catalysts were evaluated under identical conditions despite the slight variation in Au particle size. Under ambient conditions (pressure and temperature) and acidic surroundings (as demonstrated

in Figure 7a), it was observed that benzyl alcohol did not undergo degradation during the photocatalytic test. Instead, it displayed a conversion of nearly 10% (Blank Test). Furthermore, Figure 7a showcases the activity of the catalyst prepared on oxides (TiO_2 or ZrO_2), revealing strikingly different performances between the two supports. For $Au@ZrO_2$, the catalytic activity proved to be low, with a conversion of benzyl alcohol slightly above 10% (yielding less than 5% for benzaldehyde). This underperformance can be attributed to the high bandgap energy of the support (5 eV). Additionally, due to the lower energy of the light source used, electron conduction between the support and the gold NPs was impeded, therefore preventing the NPs from participating in the catalytic mechanism. In stark contrast, $Au@TiO_2$ exhibited remarkable catalytic activity, with a conversion exceeding 80%, outperforming the support, which achieved a conversion of over 55%. This highlights the active involvement of the gold NPs in the catalytic pathway. However, the selectivity of the prepared catalyst for benzaldehyde was approximately 55%, a figure close to TiO_2's selectivity of around 45%.
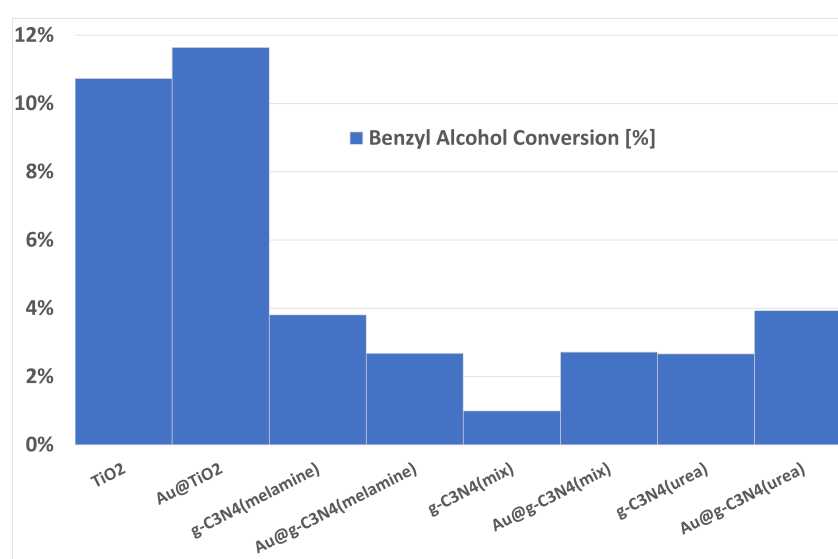
Figure 6. Dark test conducted under the following conditions: 4 h, 600 rpm, benzyl alcohol 24.7 mmol L^{-1}, 5 mL, pH = 2 (H_2SO_4), 25 mg of catalyst (Substrate:Au = 48.6 [mol:mol]), no irradiation, $P_{atm.}$, without control of the temperature.

The results obtained for the carbon nitride graphite supports, presented in Figure 7b, highlight their exceptional catalytic performance. First, all $g\text{-}C_3N_4$ supports exhibited a similar conversion exceeding 50%. However, the yields of benzaldehyde varied significantly, ranging from over 25% for $g\text{-}C_3N_{4(melamine)}$ to more than 40% for $g\text{-}C_3N_{4(urea)}$. These divergences in yields are particularly noteworthy, considering the corresponding selectivities, which ranged from 50% to 85%. Notably, the choice of the precursor was found to strongly influence the selectivity of benzaldehyde. Second, the presence of Au NPs further improved the photocatalytic performance. For example, the catalyst prepared on $g\text{-}C_3N_{4(melamine)}$ displayed an increased conversion exceeding 65%, while $Au@g\text{-}C_3N_{4(urea)}$ achieved a remarkable 75% conversion. Moreover, the influence of the $g\text{-}C_3N_4$ precursors on the selectivity for benzaldehyde remained consistent, varying from 60% for $Au@g\text{-}C_3N_{4(melamine)}$ (yield: 40%) to over 85% for $Au@g\text{-}C_3N_{4(urea)}$ (yield: more than 65%). Interestingly, the support derived from a mixture of urea and melamine demonstrated characteristics of both precursors. Based on the results, $Au@g\text{-}C_3N_{4(urea)}$ emerged as the most effective catalyst among the $g\text{-}C_3N_4$ variants. It exhibited a conversion comparable to $Au@TiO_2$ (over 75% versus over 80%). When comparing all catalysts at the same experimental condition, the carbon nitride catalyst demonstrated superior selectivity (more than 85% versus approximately 55% $Au@TiO_2$). Consequently, the final yield of benzaldehyde using carbon nitride was significantly higher (more than 65% versus approximately 45% for $Au@TiO_2$).

(**a**)

(**b**)
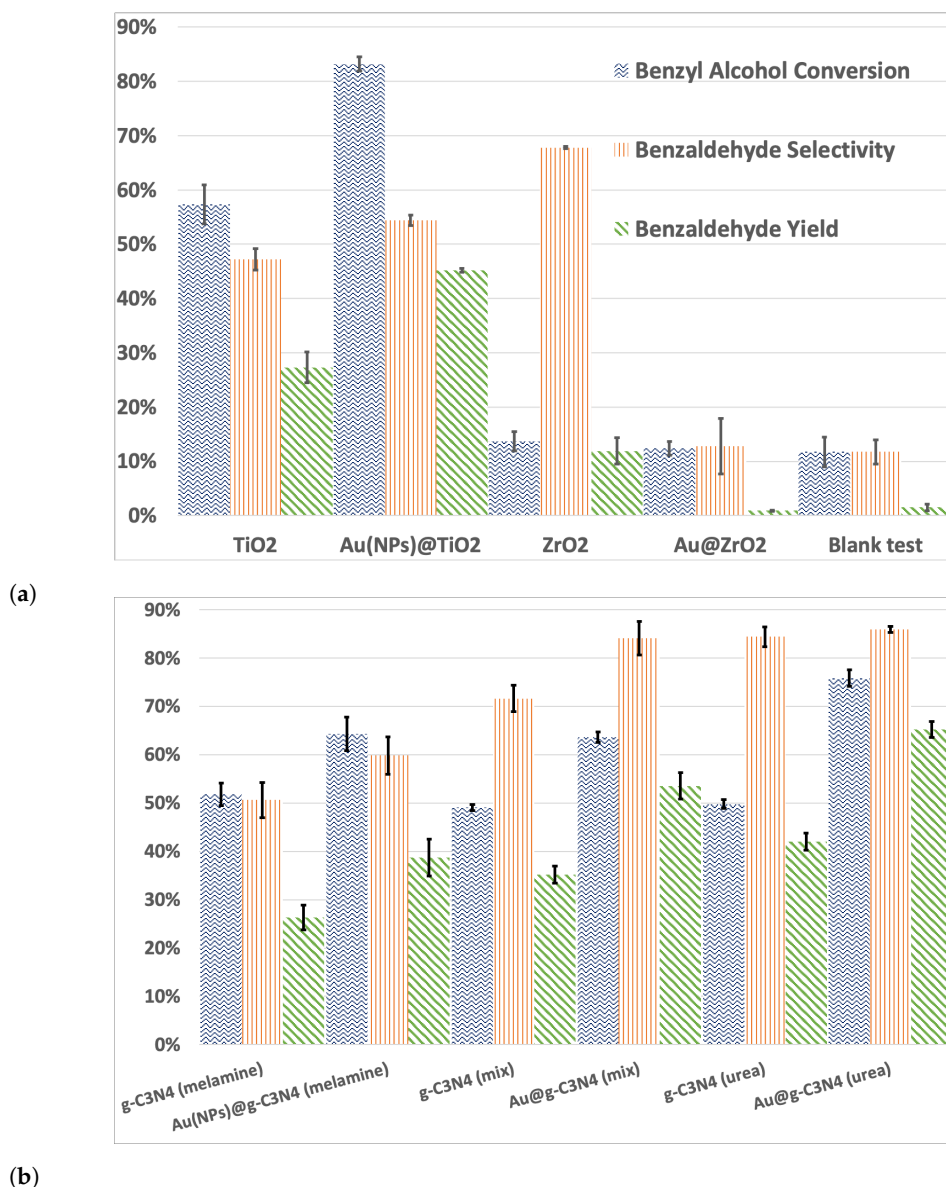
Figure 7. Photocatalytic tests results: (**a**) TiO_2 and ZrO_2 supports and based catalysts and blank test. (**b**) g-C_3N_4 supports and catalysts. The photocatalysts and the supports were tested under the same conditions: 4 h, 600 rpm, benzyl alcohol 24.7 mmol L^{-1}, 5 mL, pH = 2 (H_2SO_4), 25 mg of catalyst (Substrate:Au = 48.6 [mol:mol]), λ = 365 nm, $P_{atm.}$, without control of the temperature (after 4 h, temperature naturally increased until 40 °C).

Recycling tests for the use of Au@g-$C_3N_{4(urea)}$ catalysts in three consecutive reactions were carried out under the same conditions as those described in Section 2.12. After each cycle, the catalyst was recovered by centrifugation, washed with distilled water, and dried at 110 °C for 2h before being reused. The yield showed a slight decrease of 6%, demonstrating that the catalyst activity is stable for at least three cycles with the reaction conditions used. Furthermore, after the 3rd cycle, the recovered catalyst was analyzed by TEM and XRD to identify potential changes in crystallite and particle size. The crystallite size was also calculated using the Scherrer equation on the gold peaks before the reaction (BR) and after the recycling test (AR) of Au@g-$C_3N_{4(urea)}$ catalysts. Results show for the three angles of Au: 38° (BR 58.8 Å–AR 57.9 Å), 44° (BR 49.1 Å–AR 48.8 Å) and 64.5° (BR 62.5 Å–AR 60.1 Å) no significant change for the crystallite size. The results agree with the catalytic test.

Figure 8 shows the Au@g-C$_3$N$_{4(urea)}$ photocatalyst after 3 photocatalytic tests. In comparison with Figure 5, the particles after the test remain as dispersed as before the test, with good spreading on the surface and the presence of few aggregates (between between 15 to 25 nm). Furthermore, mean particle size did not change significantly: from 5.24 pre-test to 5.03 nm post-test (a variation of 4%), and dispersity values remained unchanged (5.24 ± 1.30 nm–5.03 ± 1.13 nm). In conclusion, photocatalytic conditions do not lead to a change in particle size or an increase in the number of aggregates.
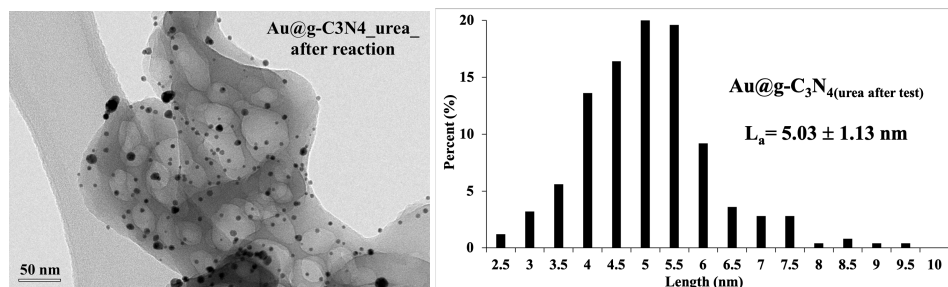

Figure 8. TEM and particles size distribution of Au@g-C$_3$N$_{4(urea)}$ after photocatalytic test.

Photocatalytic Mechanism

Gold NPs, as a metal, conduce the electrons generated by UV irradiation at a high level of energy (between the 5d band to the 6sp band [67]). This fast and high energy conduction generates hot plasmon surface electrons. This phenomenon is well known as local surface plasmon resonance (LSPR) [67,68]. Those electrons can also participate in the oxidation of the alcohol when the gold NPs are exposed to their resonance wavelength, as already presented in Section 3.4. This resonance wavelength is around 530 nm. Moreover, some tests were performed under green light irradiation, and no relevant photocatalytic activities were observed by the gold NPs. Thus, the difference in selectivity for benzaldehyde is related to the difference in the photoconduction mechanism between the two supports. Therefore, gold NPs participate in the improvement of the electron conduction. As illustrated in Figure 9, the conduction of the electrons between the gold NPs and TiO$_2$ is based on the Type-II heterojunction [68,69]. Thus, the electrons photogenerated by the gold NPs are conducted to TiO$_2$ by both conduction bands. The same mechanism applies to the photogenerated holes. However, concerning g-C$_3$N$_4$, the electron conduction is realized according to a direct Z-scheme [70]. The difference with the TiO$_2$ mechanism is the compensation of the photogenerated holes of g-C$_3$N$_4$ with the photogenerated electrons of gold NPs.

On the other hand, reported by [57], the potentials of the conduction and valence bands of TiO$_2$ and g-C$_3$N$_4$ provide a better understanding of the side reaction(s) that occur during a UV irradiation. In fact, both TiO$_2$ and g-C$_3$N$_4$ generate O$_2$ anion radicals ($-$O$_2\cdot$), which is the oxidizing species in the photooxidation of benzyl alcohol. However, the valence band of TiO$_2$ (2.7 eV vs. ENH) is sufficiently high to permit the formation of hydroxyl radicals (HO$\cdot$) (2.69 eV vs. ENH). Hydroxyl radicals are well known to be responsible for overoxidation, generating the corresponding carboxylic acid, or even complete degradation of the substrate [70]. This first approach concerning the mechanistic differences allows a better understanding of the selectivity variations for benzaldehyde between the photocatalysts based on TiO$_2$ or g-C$_3$N$_4$.
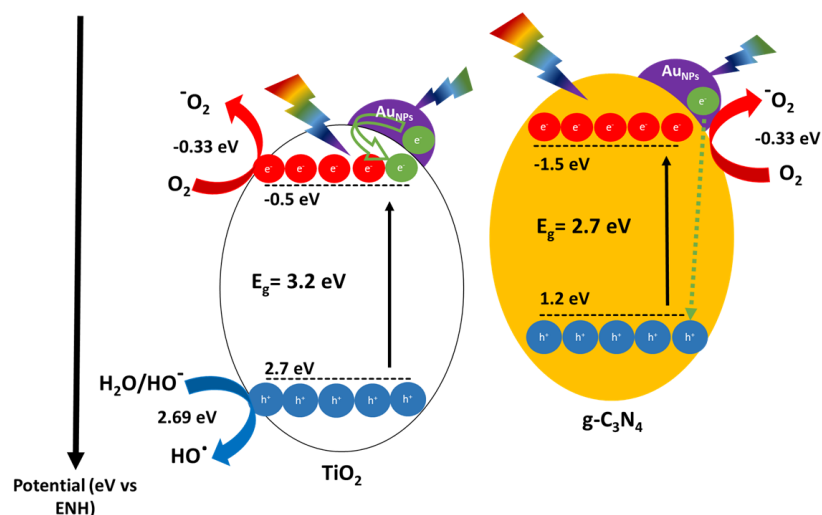
Figure 9. Illustration of the photoconduction through gold NPs supported on TiO_2 and g-C_3N_4. The potential values were obtained from [57].

4. Conclusions

The primary objective of this research was to explore alternative supports, more sustainable alternatives than metal oxides, for photocatalyst development. Graphitic carbon nitride (g-C_3N_4) was selected for this purpose due to the abundant and renewable carbon and nitrogen resources available on Earth. To assess the feasibility of replacing metal oxides with g-C_3N_4, an extensive study was conducted in the development of catalysts. Three different precursors were utilized in the synthesis of g-C_3N_4 for the immobilization of 2 wt.% of gold nanoparticles (Au NPs). Following various characterization steps, the supports and catalysts were evaluated through the selective photooxidation of benzyl alcohol into benzaldehyde. Titanium dioxide (TiO_2) and zirconium dioxide (ZrO_2) were chosen to prepare benchmark catalysts. The key findings of this study are summarized as follows: an easy catalyst preparation method was developed for Au-modified g-C_3N_4, employing new synthesis techniques involving ultrasonic baths and aqueous media. Furthermore, the study highlighted the potential to source the g-C_3N_4 precursor from sustainable resources, particularly with the use of urea. The successful synthesis of g-C_3N_4 and the effective immobilization of gold NPs were demonstrated, with some distinctions observed based on the precursor used. The catalytic performance confirmed that g-C_3N_4 catalysts exhibited better selectivity to benzaldehyde when compared to TiO_2 catalysts. Notably, the g-C_3N_4 catalyst prepared from urea exhibited the highest photocatalytic activity, achieving a substantial conversion of benzyl alcohol (75%) and the highest selectivity (85%).

To be exhaustive on the synthesis route of benzaldehyde from the benzyl alcohol oxidation, the aldehyde could be obtained by several methods such as distillation, extraction, or high conversion. The distillation seems feasible from an industrial point of view. This method takes advantage of the difference in boiling points between benzyl alcohol (bp. 205 °C) and benzaldehyde (bp. 179 °C) to separate them by fractional distillation. Another industrial process could be extraction. Indeed, benzyl alcohol and benzaldehyde have different solubilities in various solvents. Selective extraction using an appropriate solvent can be employed to separate the two compounds. This could be done in the flow process when the mixture of substrate and products is quenched in a final reactor with an adequate solvent to precipitate one of the compounds (residual benzyl alcohol, for example). Optimum reaction conditions may also be of interest. If benzyl alcohol and benzaldehyde can be selectively converted into different compounds, such as by further oxidation of benzyl alcohol to benzoic acid (or esters), separation can be achieved by exploiting the different reactivities of the products. Also, at 100% conversion, no further separation is needed.

This initial approach has made it possible to identify the feasibility of conducting the aerobic photooxidation of benzyl alcohol into benzaldehyde under mild conditions from a bio-sourced support (g-C$_3$N$_4$). Moreover, this study shows the potential of this new carbon support, with better photocatalytic properties than the usual semiconductors (TiO$_2$). Nevertheless, there is still room for improvement in achieving the green chemistry principles. Some strategies could focus on the amount of gold supported, the quantity of photocatalyst, the choice of the acid, the time of the reaction, and the type of the lighting source (switch to a polychromatic source or even sunlight).

Author Contributions: Conceptualization, L.H.; methodology, L.H., J.T.-R. and R.W.; formal analysis, L.H., M.M. and J.T.-R.; investigation, L.H., R.W., M.M. and S.H.; data curation, J.T.-R. and S.H.; writing—original draft preparation, L.H. and J.T.-R.; writing—review and editing, J.T.-R., S.H., R.W. and S.P.; visualization, J.T.-R. and R.W.; supervision, J.T.-R. and R.W.; project administration, J.T.-R.; funding acquisition, S.P. All authors have read and agreed to the published version of the manuscript.

Conflicts of Interest: The authors declare no conflict of interest.

Abbreviations

The following abbreviations are used in this manuscript:

NPs	Nanoparticules
LED	Light-Emitting Diode
FDA	Food and Drug Administration
PVA	Polyvinyl Alcohol
XRF	X-ray Fluorescence
XRD	X-ray Diffraction
ICP	Inductively Coupled Plasma
TEM	Transmission Electronic Microscopy

References

1. Vital Signs-Carbon Dioxide. Available online: https://climate.nasa.gov/vital-signs/carbon-dioxide/?_hsenc=p2ANqtz-8HpRVv9oVuSCF0VZQsQUZzqFhGtkLyw06Pme5RT0S-5vbMKKeT7887JYALC3WjAsIKVkac (accessed on 29 June 2023).
2. Cai, C.M.; Zhang, T.; Kumar, R.; Wyman, C.E. Integrated furfural production as a renewable fuel and chemical platform from lignocellulosic biomass. *J. Chem. Technol. Biotechnol.* **2014**, *89*, 2–10.
3. Wyman, V.; Henríquez, J.; Palma, C.; Carvajal, A. Lignocellulosic waste valorisation strategy through enzyme and biogas production. *Bioresour. Technol.* **2018**, *247*, 402–411.
4. De Wit, D.; Maat, L.; Kieboom, A.P.G. Carbohydrates as industrial raw materials. *Ind. Crop. Prod.* **1993**, *2*, 1–12.
5. Satrio, J.A.B.; Doraiswamy, L.K. Production of benzaldehyde: A case study in a possible industrial application of phase-transfer catalysis. *Chem. Eng. J.* **2001**, *82*, 43–56.
6. Opgrande, J.L.; Dobratz, C.J.; Brown, E.; Liang, J.; Conn, G.S.; Shelton, F.J.; With, J. Benzaldehyde. In *Kirk-Othmer Encyclopedia of Chemical Technology*; John Wiley & Sons, Inc.: Hoboken, NJ, USA, 2000.
7. Guo, C.-C.; Liu, Q.; Wang, X.-T.; Hu, H.-Y. Selective liquid phase oxidation of toluene with air. *Appl. Catal. A* **2005**, *282*, 55–59.
8. Mal, D.D.; Khilari, S.; Pradhan, D. Efficient and selective oxidation of toluene to benzaldehyde on manganese tungstate nanobars: A noble metal-free approach. *Green Chem.* **2018**, *20*, 2279–2289.
9. Shi, G.; Xu, S.; Bao, Y.; Xu, J.; Liang, Y. Selective aerobic oxidation of toluene to benzaldehyde on immobilized CoOx on SiO$_2$ catalyst in the presence of N-hydroxyphthalimide and hexafluoropropan. *Catal. Commun.* **2019**, *123*, 73–78.

10. Li, X.; Chen, Y.; Tao, Y.; Shen, L.; Xu, Z.; Bian, Z.; Li, H. Challenges of photocatalysis and their coping strategies. *Chem Catal.* **2022**, *2*, 1315–1345.

11. Fujishima, A.; Honda, K. Electrochemical photolysis of water at a semiconductor electrode. *Nature* **1972**, *238*, 37–38.

12. Regulacio, M.D.; Han, M.-Y. Multinary I-III-VI2 and I2-II-IV-VI4 semiconductor nanostructures for photocatalytic applications. *Accounts Chem. Res.* **2016**, *49*, 511–519.

13. Zhang, Z.; Qiu, C.; Xu, Y.; Han, Q.; Tang, J.; Loh, K.P.; Su, C. Semiconductor photocatalysis to engineering deuterated N-alkyl pharmaceuticals enabled by synergistic activation of water and alkanols. *Nat. Commun.* **2020**, *11*, 4722.

14. Meng, X.; Liu, L.; Ouyang, S.; Xu, H.; Wang, D.; Zhao, N.; Ye, J. Nanometals for solar-to-chemical energy conversion: From semiconductor-based photocatalysis to plasmon-mediated photocatalysis and photo-thermocatalysis. *Adv. Mater.* **2016**, *28*, 6781–6803.

15. Li, H.; Bian, Z.; Zhu, J.; Zhang, D.; Li, G.; Huo, Y.; Lu, Y. Mesoporous titania spheres with tunable chamber structure and enhanced photocatalytic activity. *J. Am. Chem. Soc.* **2007**, *129*, 8406–8407.

16. Ebadi, M.; Teymourinia, H.; Amiri, O.; Salavati-Niasari, M. Synthesis of CeO_2/Ag/Ho nanostructures in order to improve photo catalytic activity of CeO_2 under visible light. *J. Mater. Sci. Mater. Electron.* **2018**, *29*, 8817–8821.

17. Maity, P.; Mohammed, O.F.; Katsiev, K.; Idriss, H. Study of the bulk charge carrier dynamics in anatase and rutile TiO_2 single crystals by femtosecond time-resolved spectrscopy. *J. Phys. Chem. C* **2018**, *122*, 8925–8932.

18. Teng, Z.; Li, W.; Tang, Y.; Elzatahry, A.; Lu, G.; Zhao, D. Mesoporous organosilica hollow nanoparticles: Synthesis and applications. *Adv. Mater.* **2019**, *31*, 1707612.

19. Jiang, L.; Xin., B.; Yuan, F.; Wang, B.; Shi, K.; Cai, W.; Fu, H. Deactivation and regeneration of ZnO and TiO_2 nanoparticles in the gas phase photocatalytic oxidation of n-C_7H_{16} or SO_2. *Appl. Catal. A-Gen.* **2004**, *275*, 49–54.

20. Yang, H.G.; Sun, C.H.; Qiao, S.Z.; Zou, J.; Liu, G.; Smith, S.C.; Lu, G.Q. Anatase TiO_2 single crystals with a large percentage of reactive facets. *Nature* **2008**, *453*, 638–641.

21. Tachikawa, T.; Wang, N.; Yamashita, S.; Cui, S.C.; Majima, T. Design of highly sensitive fluorescent probe for interfacial electron transfer on a TiO_2 surface. *Angew. Chem. Int. Ed.* **2010**, *49*, 8593–8597.

22. Zhao, Z.; Rakheja, S.; Zhu, W.Nonvolatile reconfigurable 2D Schottky barrier transistors. *Nano Lett.* **2021**, *21*, 9318–9324.

23. Dreno, B.; Alexis, A.; Chuberre, B.; Marinovich, M. Safety of titanium dioxide nanoparticles in cosmetics. *J. Eur. Acad. Dermatol. Venereol.* **2019**, *33*, 34–46.

24. Hamad, S.; Catlow, C.R.A.; Woodley, S.M.; Lago, S.; Mejias, J.A. Structure and stability of small TiO_2 nanoparticles. *J. Phys. Chem. B* **2005**, *109*, 15741–15748.

25. Lindblad, R.; Bi, D.; Park, B.-W.; Oscarsson, J.; Gorgoi, M.; Siegbahn, H.; Odelius, M.; Johansson, E.M.J.; Rensmo, H. Electronic structure of TiO_2/$CH_3NH_3PbI_3$ perovskite solar cell interfaces. *J. Phys. Chem. Lett.* **2014**, *5*, 648–653.

26. Muqeet, M.; Gadhi, T.A.; Mahar, R.B.; Bonelli, B. Advanced nanomaterials for ultrafiltration membranes application. In *Nanomaterials for the Detection and Removal of Wastewater Pollutants*; Elsevier: Amsterdam, The Netherlands, 2020; pp. 145–160.

27. Liebig, J. Uber einige Stickstoff-Verbindungen. *Ann. Pharm.* **1834**, *10*, 1–47.

28. Zhu, J.; Xiao, P.; Li, H.; Carabineiro, S.A.C. Graphitic carbon nitride: Synthesis, properties, and applications in catalysis. *ACS Appl. Mater. Interfaces* **2014**, *6*, 16449–16465.

29. Fontelles-Carceller, O.; Muñoz-Batista, M.J.; Fernández-García, M.; Kubacka, A. Interface effects in sunlight-driven Ag/g-C_3N_4 composite catalysts: Study of the toluene photodegradation quantum efficiency. *ACS Appl. Mater. Interfaces* **2016**, *8*, 2617–2627.

30. Dette, C.; Pérez-Osorio, M.A.; Kley, C.S.; Punke, P.; Patrick, C.E.; Jacobson, P.; Giustino, F.; Jung, S.J.; Kern, K. TiO_2 anatase with a bandgap in the visible region. *Nano Lett.* **2014**, *14*, 6533–6538.

31. Thomas, A.; Fischer, A.; Goettmann, F.; Antonietti, M.; Müller, J.-O.; Schlögl, R.; Carlsson, J.M. Graphitic carbon nitride materials: Variation of structure and morphology and their use as metal-free catalysts. *J. Mater. Chem.* **2008**, *18*, 4893–4908.

32. Cao, S.; Yu, J. g-C_3N_4-based photocatalysts for hydrogen generation. *J. Phys. Chem. Lett.* **2014**, *5*, 2101–2107.

33. Zhu, Q.; Xu, Z.; Qiu, B.; Xing, M.; Zhang, J. Emerging cocatalysts on g-C_3N_4 for photocatalytic hydrogen evolution. *Small* **2021**, *17*, 2101070.

34. Al-Ahmed, A. Photocatalytic properties of graphitic carbon nitrides (g-C_3N_4) for sustainable green hydrogen production: Recent advancement. *Fuel* **2022**, *316*, 123381.

35. Zhang, M.; Yang, Y.; An, X.; Hou, L.-A. A critical review of g-C_3N_4-based photocatalytic membrane for water purification. *Chem. Eng. J.* **2021**, *412*, 128663.

36. Li, X.; Huang, G.; Chen, X.; Huang, J.; Li, M.; Yin, J.; Liang, Y.; Yao, Y.; Li, Y. A review on graphitic carbon nitride (g-C_3N_4) based hybrid membranes for water and wastewater treatment. *Sci. Total Environ.* **2021**, *792*, 148462.

37. Zhang, S.; Gu, P.; Ma, R.; Luo, C.; Wen, T.; Zhao, G.; Cheng, W.; Wang, X. Recent developments in fabrication and structure regulation of visible-light-driven g-C_3N_4-based photocatalysts towards water purification: A critical review. *Catal. Today* **2019**, *335*, 65–77.

38. Dong, F.; Zhao, Z.; Xiong, T.; Ni, Z.; Zhang, W.; Sun, Y.; Ho, W.-K. In situ construction of g-C_3N_4/g-C_3N_4 metal-free heterojunction for enhanced visible-light photocatalysis. *ACS Appl. Mater. Interfaces* **2013**, *5*, 11392–11401.

39. Xiong, T.; Cen, W.; Zhang, Y.; Dong, F. Bridging the g-C_3N_4 interlayers for enhanced photocatalysis. *ACS Catal.* **2016**, *6*, 2462–2472.

40. Yalazan, H.; Akkol, C.; Saka, E.T.; Kantekin, H. Investigation of photocatalytic properties of cobalt phthalocyanines on benzyl alcohol photoxidation. *Appl. Organomet. Chem.* **2023**, *37*, e6975.

41. Magdziarz, A.; Colmenares, J.C.; Chernyayeva, O.; Lisovytskiy, D.; Grzonka, J.; Kurzydłowski, K.; Freindl, K.; Korecki, J. Insight into the synthesis procedure of Fe^{3+}/TiO_2-based photocatalyst applied in the selective photo-oxidation of benzyl alcohol under sun-imitating lamp. *Ultrason. Sonochem.* **2017**, *38*, 189–196.

42. Zhang, H.; Li, X.; Chooi, K.S.; Jaenicke, S.; Chuah, G.-K. TiO_2 encapsulated Au nanostars as catalysts for aerobic photo-oxidation of benzyl alcohol under visible light. *Catal. Today* **2021**, *375*, 558–564.

43. Li, S.; Cai, J.; Wu, X.; Zheng, F. Sandwich-like $TiO_2@$ ZnO-based noble metal (Ag, Au, Pt, or Pd) for better photo-oxidation performance: Synergistic effect between noble metal and metal oxide phases. *Appl. Surf. Sci.* **2018**, *443*, 603–612.

44. Li, S.; Cai, J.; Wu, X.; Liu, B.; Chen, Q.; Li, Y.; Zheng, F. $TiO_2@ Pt@CeO_2$ nanocomposite as a bifunctional catalyst for enhancing photo-reduction of Cr (VI) and photo-oxidation of benzyl alcohol. *J. Hazard. Mater.* **2018**, *346*, 52–61.

45. Tamiolakis, I.; Lykakis, I.N.; Armatas, G.S. Mesoporous CdS-sensitized TiO_2 nanoparticle assemblies with enhanced photocatalytic properties: Selective aerobic oxidation of benzyl alcohols. *Catal. Today* **2015**, *250*, 180–186.

46. Klaassen, C.D.; Liu, J.; Diwan, B.A. Metallothionein protection of cadmium toxicity. *Toxicol. Appl. Pharmacol.* **2009**, *238*, 215–220.

47. Yang, Z.; Xu, X.; Liang, X.; Lei, C.; Cui, Y.; Wu, W.; Yang, Y.; Zhang, Z.; Lei, Z. Construction of heterostructured MIL-125/Ag/g-C_3N_4 nanocomposite as an efficient bifunctional visible light photocatalyst for the organic oxidation and reduction reactions. *Appl. Catal. B* **2017**, *205*, 42–54.

48. Akhtar, B.; Ghafuri, H.; Rashidizadeh, A. Synergistic effect of iodine doped TiO_2 nanoparticle/g-C_3N_4 nanosheets with upgraded visible-light-sensitive performance toward highly efficient and selective photocatalytic oxidation of aromatic alcohols under blue LED irradiation. *Mol. Catal.* **2021**, *506*, 111527.

49. Ferraz, C.P.; Zieliński, M.; Pietrowski, M.; Heyte, S.; Dumeignil, F.; Rossi, L.M.; Wojcieszak, R. Influence of Support Basic Sites in Green Oxidation of Biobased Substrates Using Au-Promoted Catalysts. *ACS Sustain. Chem. Eng.* **2018**, *6*, 16332–16340.

50. Al Rawas, H. K.; Ferraz, C. P.; Thuriot-Roukos, J.; Heyte, S.; Paul, S.; Wojcieszak, R. Influence of Pd and Pt Promotion in Gold Based Bimetallic Catalysts on Selectivity Modulation in Furfural Base-Free Oxidation. *Catalysts* **2021**, *11*, 1226.

51. Rojas, S.D.; Espinoza-Villalobos, N.; Salazar, R.; Escalona, N.; Contreras, D.; Melin, V.; Laguna-Bercero, M.A.; Sánchez-Arenillas, M.; Vergara, E.; Caceres-Jensen, L. Selective photocatalytic conversion of guaiacol using g-C_3N_4 metal free nanosheets photocatalyst to add-value products. *J. Photochem. Photobiol. A* **2021**, *421*, 113513.

52. Saravanakumar, K.; Velmurugan Shanmuga, P.; Vellaichamy, B.; Seenivasan Lakshmi, P.; Velluchamy, M. Noble metal nanoparticles (Mx = Ag, Au, Pd) decorated graphitic carbon nitride nanosheets for ultrafast catalytic reduction of anthropogenic pollutant, 4-nitrophenol. *Environ. Res.* **2022**, *212*, 113185.

53. Monti, E.; Ventimiglia, A.; Soto, C.A.G.; Martelli, F.; Rodríguez-Aguado, E.; Cecilia, J. A.; Maireles-Torres, P.; Ospitali, F.; Tabanelli, T.; Albonetti, S.; et al. Oxidative condensation/esterification of furfural with ethanol using preformed Au colloidal nanoparticles. Impact of stabilizer and heat treatment protocols on catalytic activity and stability. *Mol. Catal.* **2022**, *528*, 112438.

54. Lima, M.J.; Tavares, P.B.; Silva, A.M.T.; Silva, C.G.; Faria, J.L. Selective photocatalytic oxidation of benzyl alcohol to benzaldehyde by using metal-loaded g-C_3N_4 photocatalysts. *Catal. Today* **2017**, *287*, 70–77.

55. Dercz, A.; Prusik, K.; Pająk, K. X-ray and SEM studies on zirconia powders. *J. Ach. Mat. Manuf. Eng.* **2008**, *31*, 408–414.

56. Krusberski, N. Exploring potential errors in XRF analysis. *J. S. Afr. Inst. Min. Metall.* **2006**, 1–8.

57. Wen, J.; Xie, J.; Chen, X.; Li, X. A review on g-C_3N_4-based photocatalysts. *Appl. Surf. Sci.* **2017**, *391*, 72–123.

58. Wang, X.; Maeda, K.; Thomas, A.; Takanabe, K.; Xin, G.; Carlsson, J.M.; Domen, K.; Antonietti, M. A metal-free polymeric photocatalyst for hydrogen production from water under visible light. *Nat. Mater.* **2009**, *8*, 76–80.

59. Zhu, B.; Xia, P.; Ho, W.; Yu, J. Isoelectric point and adsorption activity of porous g-C_3N_4. *Appl. Surf. Sci.* **2015**, *344*, 188–195.

60. Linh, P.H.; Do Chung, P.; Van Khien, N.; Bach, T.N.; Hang, L.T.; Hung, N.M.; Van Thanh, D. A simple and green photoreduction approach for synthesis of Au/g−C_3N_4 hybrid nanocomposites with high solar light photocatalytic activity. *Semicond. Sci. Technol.* **2022**, *37*, 035002.

61. Colmenares, J.C.; Ouyang, W.; Ojeda, M.; Kuna, E.; Chernyayeva, O.; Lisovytskiy, D.; De, S.; Luque, R.; Balu, A. M. Mild ultrasound-assisted synthesis of TiO_2 supported on magnetic nanocomposites for selective photo-oxidation of benzyl alcohol. *Appl. Catal. B* **2016**, *183*, 107–112.

62. Taghavi, S.; Amoozadeh, A.; Nemati, F. The first report of deep eutectic solvent (DES) nano-photocatalyst (n-TiO_2-P25@ TDI@ DES (urea: $ZnCl_2$)) and its application on selective oxidation of benzyl alcohols to benzaldehydes. *J. Chem. Technol. Biotechnol.* **2021**, *96*, 384–393.

63. Dai, Y.; Tüysüz, H.Rapid acidic media growth of $Cs_3Bi_2Br_9$ halide perovskite platelets for photocatalytic toluene oxidation. *Sol. RRL* **2021**, *5*, 2100265.

64. Anastas, P.; Eghbali, N. Green chemistry: Principles and practice. *Chem. Soc. Rev.* **2009**, *39*, 301–312.

65. Chang, C.; Fu, Y.; Hu, M.; Wang, C.; Shan, G.; Zhu, L. Photodegradation of bisphenol A by highly stable palladium-doped mesoporous graphite carbon nitride (Pd/mpg-C_3N_4) under simulated solar light irradiation. *Appl. Catal. B* **2013**, *142*, 553–560.

66. Yan, S.C.; Li, Z.S.; Zou, Z.G. Photodegradation performance of g-C_3N_4 fabricated by directly heating melamine. *Langmuir* **2009**, *25*, 10397–10401.

67. Sarina, S.; Waclawik, E. R.; Zhu, H. Photocatalysis on supported gold and silver nanoparticles under ultraviolet and visible light irradiation. *Green Chem.* **2013**, *7*, 1814–1833.

68. Amendola, V.; Pilot, R.; Frasconi, M.; Maragò, O. M.; Iatì, M. A. Surface plasmon resonance in gold nanoparticles: A review. *J. Phys. Condens. Matter* **2017**, *29*, 203002.
69. Leong, K.H. Development of Modified Titania Nano Photocatalysts to Synergise Visible Light Utilisation for Enhanced Photocatalysis. Ph.D. Thesis, University of Malaya, Kuala Lumpur, Malaysia, 2015.
70. Low, J.; Jiang, C.; Cheng, B.; Wageh, S.; Al-Ghamdi, A.A.; Yu, J. A review of direct Z-scheme photocatalysts. *Small Methods* **2017**, *1*, 1700080.